Title

A mitochondria-targeting lipid–small molecule hybrid nanoparticle for imaging and therapy in an orthotopic glioma model

Journal

Acta Pharmaceutica Sinica B, 12(6)

ISSN

2211-3835

Authors

Tang, Menghuan
Lin, Kai
Ramachandran, Mythili
et al.

Publication Date

2022-06-01

DOI

10.1016/j.apsb.2022.04.005

Peer reviewed

Acta Pharmaceutica Sinica B 2022;12(6):2672–2682

Chinese Pharmaceutical Association
Institute of Materia Medica, Chinese Academy of Medical Sciences

Acta Pharmaceutica Sinica B

www.elsevier.com/locate/apsb
www.sciencedirect.com

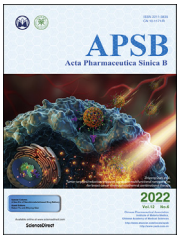

ORIGINAL ARTICLE

A mitochondria-targeting lipid–small molecule hybrid nanoparticle for imaging and therapy in an orthotopic glioma model

Menghuan Tang[a,b], Kai Lin[b,d], Mythili Ramachandran[b], Longmeng Li[b], Hongye Zou[b], Huzhi Zheng[a], Zhao Ma[b,c,*], Yuanpei Li[b,*]

[a]*Key Laboratory of Luminescent and Real-Time Analytical Chemistry, Ministry of Education, College of Chemistry and Chemical Engineering, Southwest University, Chongqing 400715, China*
[b]*Department of Biochemistry and Molecular Medicine, UC Davis School of Medicine, Sacramento, CA 95817, USA*
[c]*Department of Medicinal Chemistry, Key Laboratory of Chemical Biology (MOE), School of Pharmaceutical Sciences, Cheeloo College of Medicine, Shandong University, Jinan 250012, China*
[d]*College of Food Science and Engineering, Ocean University of China, Qingdao 266003, China*

Received 1 December 2021; received in revised form 7 March 2022; accepted 31 March 2022

KEY WORDS

Lipid-small molecule nanoparticle;
Hybrid nanoparticle;
Mitochondria targeting;
Photodynamic therapy;
Orthotopic glioma;
Tumor imaging;
Drug delivery;
Cancer therapy

Abstract Hybrid lipid–nanoparticle complexes have shown attractive characteristics as drug carriers due to their integrated advantages from liposomes and nanoparticles. Here we developed a kind of lipid-small molecule hybrid nanoparticles (LPHNPs) for imaging and treatment in an orthotopic glioma model. LPHNPs were prepared by engineering the co-assembly of lipids and an amphiphilic pheophorbide a–quinolinium conjugate (PQC), a mitochondria-targeting small molecule. Compared with the pure nanofiber self-assembled by PQC, LPHNPs not only preserve the comparable antiproliferative potency, but also possess a spherical nanostructure that allows the PQC molecules to be administrated through intravenous injection. Also, this co-assembly remarkably improved the drug-loading capacity and formulation stability against the physical encapsulation using conventional liposomes. By integrating the advantages from liposome and PQC molecule, LPHNPs have minimal system toxicity, enhanced potency of photodynamic therapy (PDT) and visualization capacities of drug biodistribution and tumor imaging. The hybrid nanoparticle demonstrates excellent curative effects to significantly prolong the survival of mice with the orthotopic glioma. The unique co-assembly of lipid and small molecule provides new potential for constructing new liposome-derived nanoformulations and improving cancer treatment.

*Corresponding authors.
E-mail addresses: mazhao@sdu.edu.cn (Zhao Ma), lypli@ucdavis.edu (Yuanpei Li).

Peer review under responsibility of Chinese Pharmaceutical Association and Institute of Materia Medica, Chinese Academy of Medical Sciences.

https://doi.org/10.1016/j.apsb.2022.04.005

1. Introduction

Liposomes are lipid-based small vesicles that are composed of at least one lipid bilayer surrounding the aqueous core[1,2]. This characteristic of liposomes mimics the shape of natural cellular compartments and they have minimal toxicity, high level of biocompatibility and biodegradability[3−5]. The amphiphilic structure of liposomes allows them to entrap both hydrophilic and hydrophobic drugs, making them excellent candidates for drug delivery platforms[6,7]. Although liposomes have many intrinsic advantages, poor stability and low drug loading capacity of conventional liposomes limit their efficacy, thus needing further optimization[8−10]. Recently, hybrid lipid−nanoparticle complexes (HLNCs) have emerged as a new generation of drug delivery systems[11−13]. These hybrids are engineered to integrate the excellent properties of nanoparticles, such as high stability and ease of functionalization, with good biocompatibility and low toxicity of liposomes. For instance, solid lipid nanoparticles entrapping inorganic nanoparticles, like Au nanoparticles and polymetric lipid hybrid nanoparticles entrapping polymers, such as polylactic acid, both exhibited improved stability and potential application in bioimaging and drug delivery[12,14−16]. Since lipid-based hybrid nanoparticles have many integrated advantages, it is promising to utilize lipid on other nanomaterials for improved formulation to achieve enhanced therapeutic effect.

Recently, small molecule self-assembled nanomaterials in which single or multiple drug molecules serve as both building blocks and cargos have been engineered as a promising candidate for drug delivery[17−19]. Compared to the conventional nanoscale drug delivery system, small molecule-assembled nanomaterials exhibit improved features, such as higher drug loading efficiency and a simple formulation process[20]. Our group has developed a mitochondria targeting photosensitizer (PQC NFs) capable of forming nanofibers (NFs) through the self-assembly of amphiphilic pheophorbide a−quinolinium conjugate (PQC)[21]. PQC NFs exhibit specific accumulation in mitochondria and can be retained within tumor sites *in vivo* for 10 days. As a consequence, PQC NFs could achieve a powerful tumor ablation effect in both subcutaneous and orthotopic oral cancer models with only a single dose of treatment. Unfortunately, due to the nanofiber structure, PQC NFs were unable to be administrated by intravenous injection (i.v.), which limits its application to other tumor types and its clinical translation.

Herein, we report a kind of mitochondria-targeting lipid-small molecule hybrid nanoparticles (LPHNPs) which were constructed by the co-assembly of lipids and PQC. Different from PQC NFs, LPHNPs exhibited a spherical nanostructure and desirable particle size, which reduced the potential systemic toxicity and enabled the nanoparticles to be administered *via* i.v. injection (Fig. 1). In addition, LPHNPs showed a higher loading capacity and better stability compared to conventional liposomes and preserved the excellent properties of PQC, such as mitochondria targeting, fluorescent imaging capability, and photosensitization. Notably, LPHNPs achieved excellent *in vivo* imaging ability, and potent therapeutic effects in an orthotopic glioma model in immune competent mice. The simple preparation procedure, admirable PDT therapeutic effect, and optical imaging ability make this hybrid nanoparticle an ideal candidate for imaging and treatment of glioma.

2. Materials and methods

2.1. Chemicals

Pheophorbide a (PA) was bought from Santa Cruz Biotechnology (TX, USA). L-α-Phosphatidylcholine was purchased from Avanti Polar Lipids, Inc (AL, USA). Cholesterol was brought from MP Biomedicals (OH, USA). mPEG-DSPE (MW: 2000) was brought from Laysan Bio, Inc (AL, USA). Organic solvents were purchased from Fisher Scientific (MA, USA).

2.2. Preparation of NPs

PQC molecule was synthesized according to our previous report[21]. LPHNPs and PA@liposome were prepared *via* a classical thin-film hydration method[22,23]. Briefly, L-α-phosphatidylcholine (EPC, 10 mg), cholesterol (2.2 mg), mPEG-DSPE (2.2 mg) and PQC (1 mg) or PA (1 mg) were dissolved in chloroform and added into a round-bottom flask under stirring. Then, the chloroform was evaporated to form a thin film. 1 mL phosphate-buffered saline (PBS) was added to re-hydrate the thin film, followed by low-level shaking overnight.

2.3. Characterization of NPs

UV−vis spectra were obtained with a UV−vis spectrometer (UV-1800, Shimadzu). Fluorescence spectra were collected by a fluorescence spectrometer (RF-6000, Shimadzu) with the excitation wavelength at 412 nm. Size distribution, PDI and zeta potential were measured by dynamic light scattering (DLS; Malvern, Nano-ZS). The morphology of nano-assemblies was observed by a Talos L120C TEM (Thermo Fisher, USA) at an accelerating voltage of 80 kV. To calculate the drug loading rate, a standard curve between a series of free PQC or PA solutions and the absorbance at 410 nm was generated. Nano-assemblies were filtered by the centrifugal centrifuge columns (MWCO: 10 kDa) and the absorbance of the filtrate was measured.

2.4. Cell culture

The original and transfected GL261 and U251 cells were kindly provided by Dr. Kit Lam's lab. The U118 and IMR-90 cells were obtained from ATCC. U118 and U251 cells were cultured in Dulbecco's modified Eagle medium (DMEM), containing 10% FBS and 1% penicillin/streptomycin. IMR-90 cells were cultured in Eagle's minimum essential medium (EMEM), containing 10% FBS and 1% penicillin/streptomycin. GL261 cells were maintained in the Gibco Dulbecco's modified Eagle medium: Nutrient Mixture F-12 (DMEM/F-12), containing 1 × ITS (Insulin-Transferrin-Selenium) Liquid Media supplement (Sigma, USA), 1 × MEM Non-Essential Amino Acids (Thermofisher, USA), 1 ×

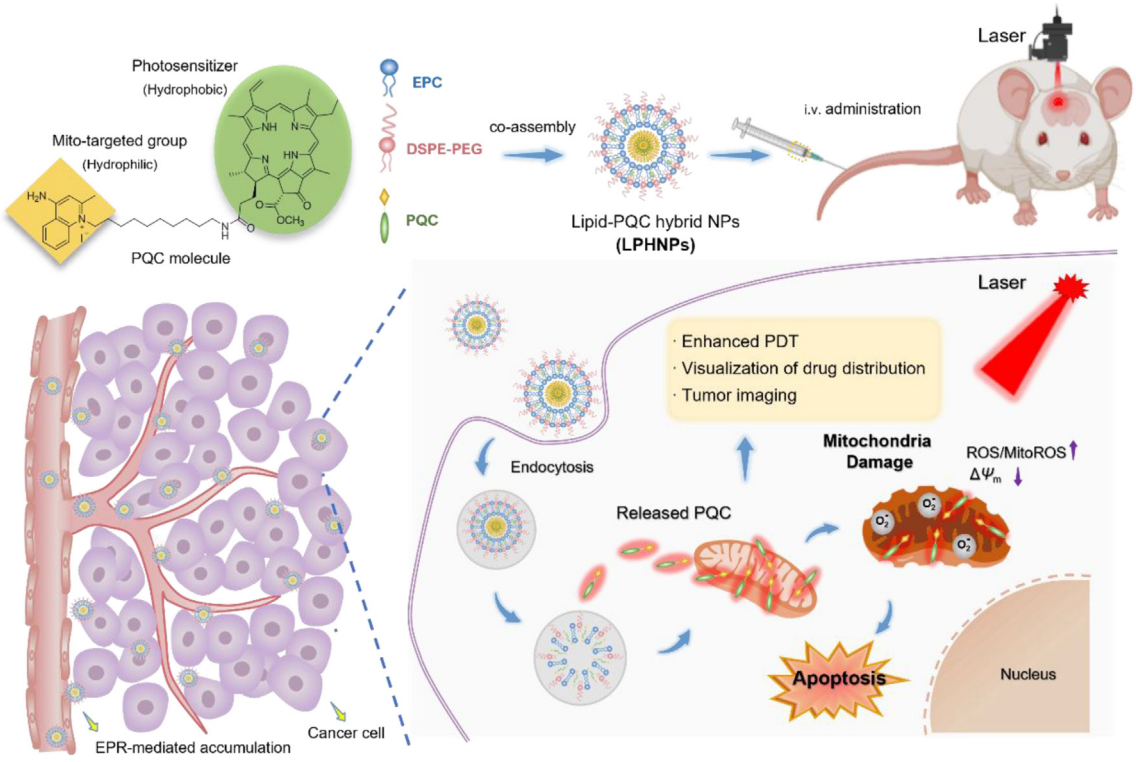

Figure 1 Schematic illustration of hybrid nanoparticles (LPHNPs) based on amphiphilic lipids and mitochondria targeting PQC molecules.

GlutaMAXTM (Thermofisher, USA), 10% FBS and 1% penicillin/streptomycin. All cells were incubated at 37 °C in a fully humidified atmosphere of 5% CO_2 in the air.

2.5. *Cell viability assay*

GL261, U251, U118 and IMR-90 cells (5×10^3 cells/well) were plated in 96-well plates, incubated overnight, and then treated with different concentrations of agents as indicated. After 24 h treatment, the cells were washed and cultured with fresh medium. For the light treated groups, cells were irradiated for 30 s using a 633-nm LED array (Omnilux new-U, power density: 30 mW/cm^2) and further incubated for 24 h in parallel with the non-light treated group. Cell viability was quantified using the CellTiter-Glo assay (Promega, USA) and the luminescence intensity was measured by a microplate reader (Molecular Devices, SpectraMax iD5, USA).

2.6. *Cell uptake assay*

GL261 cells (5×10^3 cells/well) were seeded in a 96-well plate, incubated overnight for full attachment, and treated with 1 μmol/L of agents at different time points as indicated. At the end of the experiment, cells were lysed with dimethyl sulfoxide (DMSO). Fluorescence intensity (Ex = 412 nm, Em = 675 nm) was measured by a microplate reader (Tecan, Switzerland).

2.7. *Colocalization assay*

To conduct the subcellular localization assays, GL261 cells were incubated in a cell view dish overnight and treated with LPHNPs or PA@liposome (1 μmol/L) for 24 h, followed by staining with MitoTracker Green (Cell Signaling Technology, USA) for 1 h and Hoechst 33342 (Thermo Fisher Scientific, USA) for 15 min. Cells were visualized using a confocal laser scanning microscopy (CLSM; Carl Zeiss, Germany). Signals of LPHNPs or PA@liposome were observed under the Cy5 channel, MitoTracker were observed under the Alexa Fluor 488 channel and Hoechst 33342 were observed under Hoechst 33342 channel. The corresponding Pearson's correlation coefficient was calculated by ImageJ Fiji.

2.8. *Mitochondrial membrane potential analysis*

JC-1 dye (Thermo Fisher Scientific, USA) was used as an indicator of mitochondrial membrane potential. Briefly, cells (2×10^4 cells/well) were treated as indicated for 24 h, washed and cultured with fresh medium. For the light treated group, cells were irradiated for 30 s using a 633-nm LED array (30 mW/cm^2) and incubated for 2 h. Then 0.5 μg/mL JC-1 was added for another 30 min of incubation. Meanwhile, Hoechst 33342 (0.1 μg/mL) was added and incubated for 15 min. Images were captured by CLSM. The ratio of red/green fluorescence intensity was calculated by ImageJ Fiji.

2.9. *Electron microscopy*

GL261 cells seeded at 2×10^4 cells/well in 8-well slide plates (Thermo Fisher, USA) were incubated overnight, treated as indicated for 24 h and then washed with PBS. For the light treated group, cells were incubated with fresh medium and were treated with light for 30 s. After another 2 h of incubation, cells were fixed with the 0.1 mol/L cacodylate buffer containing 2.5%

glutaraldehyde plus 2% paraformaldehyde, and transferred to the carbon square mesh, followed by observation using the Talos L120C TEM.

2.10. ROS/MitoROS production assay in cellular level

GL261 cells (1.0×10^6 cells/well) were seeded in 96-well plates and cultured for 24 h. The cells were treated with 1 μmol/L LPHNPs or PA@liposome NPs for 24 h. After washing with PBS, the cells were incubated with DCF-DA (10 μmol/L) probe for 30 min, followed by light treatment (633-nm LED array, 30 mW/cm^2) for 30 s. Cells were collected and analyzed by flow cytometry (Guava easyCyte Flow Cytometer, MilliporeSigma, USA). Data analysis was accomplished using guavaSoft 3.3 software. For CLSM, cells were treated as above and were incubated with DCF-DA (10 μmol/L) and 1 × MitoROS™ 580 (AAT Bioquest, Inc., USA) probe for 30 min, followed by light treatment (633-nm LED array, 30 mW/cm^2) for 30 s. Cells were incubated for 30 min and then observed by CLSM.

2.11. Apoptosis assay

GL261 cells (5×10^5 cells/well) were seeded in 6-well plates and cultured for 24 h. The cells were treated with 0.5 μmol/L LPHNPs or PA@liposome NPs for 24 h. After washing with PBS, the cells were incubated with fresh media and irradiated for 30 s (633-nm LED array, 30 mW/cm^2), and were cultured for another 24 h. Cells were collected and stained with the apoptosis kit (Annexin V-FITC/propidium iodide, Biolegend, USA) according to the manufacturer's instructions. All samples were immediately analyzed by flow cytometry (Guava easyCyte Flow Cytometer, MilliporeSigma, USA) after staining. Data analysis was accomplished using guavaSoft 3.3 software.

2.12. Animal model

All animal experiments were carried out in accordance with guidelines and animal protocol approved by the ethics committee of the University of California, Davis, USA. Female C57BL/6 mice (6 weeks old) were purchased from Harlan (Livermore, CA, USA) for orthotopic model establishment. 2 μL of GL261 cells (5×10^5 cells) were injected into the right striatum of the mouse. Animals received post-surgery pain management for 3 days.

2.13. In vivo/ex vivo fluorescence imaging

C57BL/6 mice bearing orthotopic GL261 tumors were subjected to tail vein injection of LPHNPs (10 mg/kg). Mice were injected with D-luciferin (150 μL of 20 mg/mL) and imaged using Lago X (Spectral Instruments Imaging, USA) at designated time points. After 24 h of injection, mice were sacrificed, and their organs including the brain with tumor were harvested for *ex vivo* imaging. The whole brain bearing a tumor was immersed with optimum cutting temperature (O.C.T.) compound and frozen at −80 °C, and then cut into 10 μmol/L thick cryo-sections for fluorescence imaging. The corresponding Pearson's correlation coefficient was calculated by ImageJ Fiji.

2.14. In vivo antitumor studies

One week after tumor implantation, C57BL/6 mice bearing orthotopic GL261 tumors were randomly divided into three groups: PBS, LPHNPs and PA@liposome. LPHNPs and PA@liposome (10 mg/kg) were injected *via* tail vein for one dose on Day 0. For the light treated groups, the right side of the brain was irradiated with a NIR laser system (Shanghai Xilong Optoelectronics Technology, China) at 680 nm at 0.2 W/cm^2 for 3 min after 24 and 48 h of drug administration. Tumor growth was monitored over time by recording bioluminescence signals (mouse was injected with 150 μL of 20 mg/mL D-luciferin) using Lago X (Spectral Instruments Imaging, USA). At the end of experiment, mice were sacrificed, and the tumors were harvested for histopathology analysis.

2.15. Statistical analysis

The experimental data were statistically analyzed using the GraphPad Prism 7.0. Data were reported as the mean ± standard deviations (SD). Data statistics were analyzed by calculating the *t*-test between two groups. ns.: not significant; $^*P < 0.05$; $^{**}P < 0.01$; $^{***}P < 0.001$; $^{****}P < 0.0001$.

3. Results and discussion

3.1. Preparation and characterization of the LPHNPs

As we presented previously, PQC molecule, the active pharmaceutical ingredient that targets mitochondria tends to form nanofibrils (PQC NFs), which is conducive to the retention in tumor of agents but not to their blood circulation (Fig. 2A and C)[21]. To adjust and optimize the micromorphology of PQC nanoassemblies, we introduced an amphiphilic lipid (L-α-phosphatidylcholine) for co-assembly. The typical thin-film hydration method was utilized to prepare LPHNPs (Fig. 2B). Transmission electron microscopy (TEM) studies showed that LPHNPs have a uniform and typical core-shell vesicular microstructure (Fig. 2D). This result is consistent with the dynamic light scattering (DLS) measurements, by which the hydrodynamic size, polydispersity index (PDI), and surface charge of LPHNPs were determined to be ∼54.3 nm, ∼0.26 and −1.9 mV, respectively (Fig. 2E). To better elucidate the superiority of the hybrid nanoparticle, we also made a conventional nanoformulation (PA@liposome) that physically loads the hydrophobic PA in liposomes. Under the same drug loading content with LPHNPs, PA@liposome displayed irregular microstructures with several cavities and uneven thickness of films despite the similar DLS result to that of LPHNPs (Fig. 2G and H). This is likely due to the high hydrophobicity and strong $\pi-\pi$ stacking of PA as well as the resulting varied aggregation and distribution in the hydrophobic bilayer. It should be noted that compared with the high-positively charged PQC NFs (∼40 mV) and high-negatively charged PA@liposome, LPHNPs displayed a neutral surface charge (Supporting Information Fig. S1a), which reflects that the interaction between the lipids and PQC molecules on the surface of nano-assemblies (Fig. 2B). Co-assembly of lipids with PQC qualified a high drug loading capacity (up to 55%) with an excellent encapsulation efficiency (92%), which can be attributed to the amphiphilic property and co-assembly of PQC and lipids (Fig. S1b). In addition, LPHNPs were stable in the long-term (one week) storage condition or in the presence of 10% serum (Fig. 2F and Fig. S1c). At 10% loading rate, PA@liposome also showed stability for over one week or in PBS with 10% serum (Fig. 2I and Fig. S1d). However, PA@liposome precipitated after one-week storage when the loading rate increased to 20%

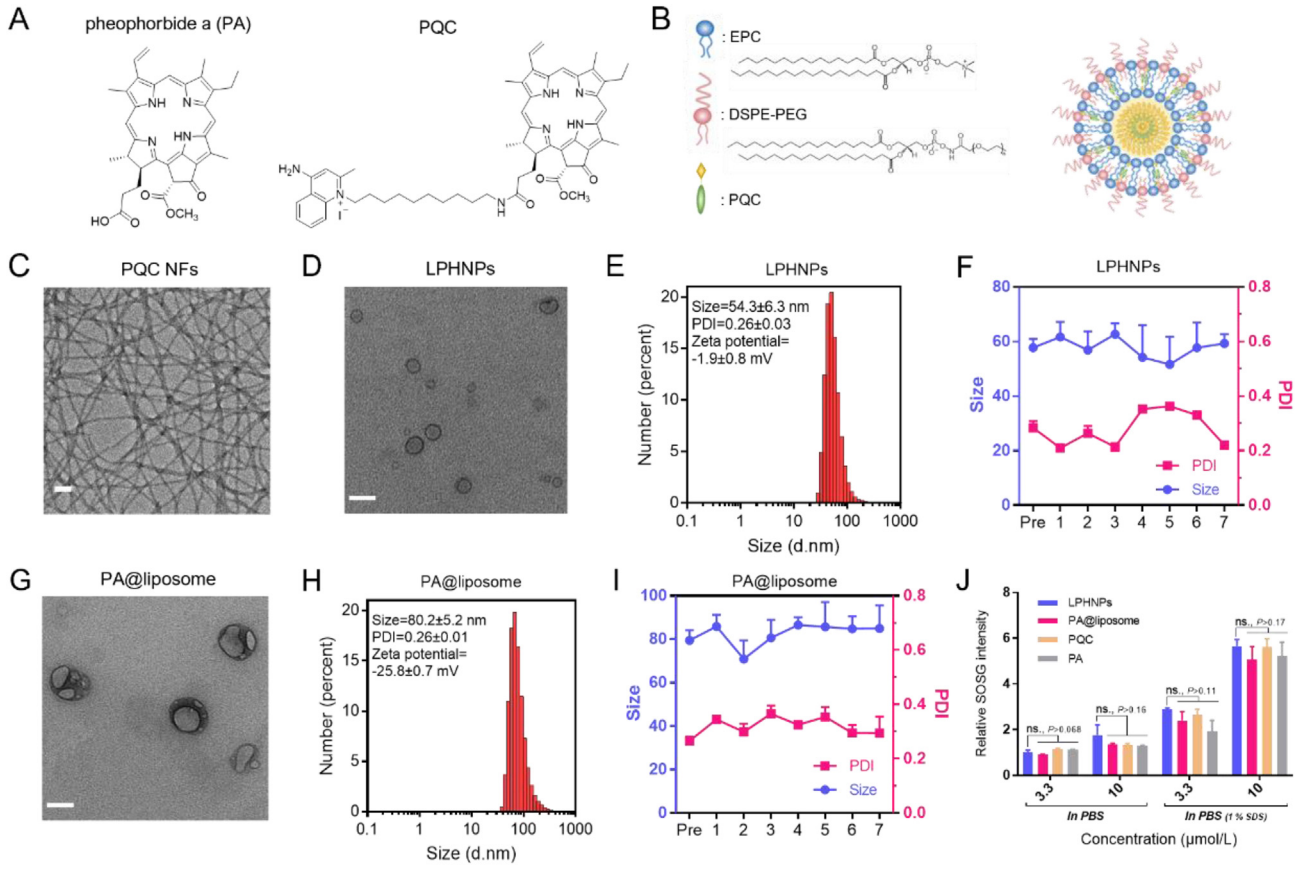

Figure 2 (A) Chemical structures of PA and PQC. (B) Schematic synthesis of LPHNPs. (C, D) Representative TEM images of PQC NFs (C) and LPHNPs (D). Scale bar = 50 nm. (E) DLS analysis of LPHNPs. (F) Stability of LPHNPs in PBS for 7 days. (G) Representative TEM image of PA@liposome. Scale bar = 50 nm. (H) DLS analysis of PA@liposome. (I) Stability of PA@liposome in PBS for 7 days. (J) $^1O_2$ production levels of different formulations of PQC or PA in the aggregation (PBS) and dissociation (PBS/SDS) forms with SOSG as an $^1O_2$ indicator. The mentioned PBS/SDS solution contains 1% SDS (*w*/*v*) which was used to disrupt nanoparticles. Values are mean ± SD. Statistical analysis was performed with *t*-test. ns., not significant.

(Fig. S1e). Overall, LPHNPs exhibited a notable advantage over the traditional liposome formulations.

3.2. *Optical and photodynamic properties*

We next investigated the optical properties for further understanding the co-assembly details of lipids and PQC molecules. As shown in Supporting Information Fig. S2a and b, similar to that of PA@liposome, the fluorescence of LPHNPs was quenched in the aggregation state (intact nanoparticle), while recovered in the free state (dissociated nanoparticle) when the nanoparticles were dissociated by sodium dodecyl sulfate (SDS). As previously shown, PA is a typical fluorophore with aggregation-caused quenching (ACQ) property[24–26]. The fluorescence quenching behavior of LPHNPs indicates that the strong hydrophobicity interaction and $\pi-\pi$ stacking of PA play an essential role in the co-assembly. Moreover, the near-infrared (NIR) fluorescence imaging studies demonstrated inactivated fluorescence of aggregated photosensitizer and the discernible fluorescence of free photosensitizer (Fig. S2c). This is consistent with the aforementioned findings. Subsequently, the photodynamic efficiency was evaluated by using the singlet oxygen sensor green (SOSG) as an $^1O_2$ indicator[27]. It was found that in the same medium, different formulations of PQC and PA produced an equivalent level of $^1O_2$. This result not only indicates that the PQC and PA with the same photosensitization group have the equivalent photodynamic efficiency but also implies that the co-assembly with lipids did not hinder the $^1O_2$ generating capacity of PQC (Fig. 2J). In addition, the free PQC or PA molecules (in SDS/PBS) produced significantly increased levels of $^1O_2$ than their aggregated forms (in pure PBS), which is consistent with the fluorescence performance and our previous findings[21].

3.3. *Cellular uptake and cell viability*

Cellular uptake of LPHNPs was assessed by using GL261, a murine glioma cell line. As shown in Fig. 3A, LPHNPs showed a rapid accumulation inside cells over time, and their cellular concentrations at predetermined time points are significantly higher than those of PA@liposome, respectively. This is because of the neutral surface charge of LPHNPs in contrast to the negative charge on the surface of conventional liposomes[28,29]. Cell viability assays were then carried out to ascertain the anticancer effects against GL261 cells, and the results are presented in Fig. 3B. In the absence of light irradiation, PA@liposome and free PA exhibited a neglectable anti-GL261 effect ($IC_{50} > 90$ μmol/L), while LPHNPs and PQC NFs were more potent by showing their IC_{50} at approximately 3 μmol/L (Supporting Information Fig.

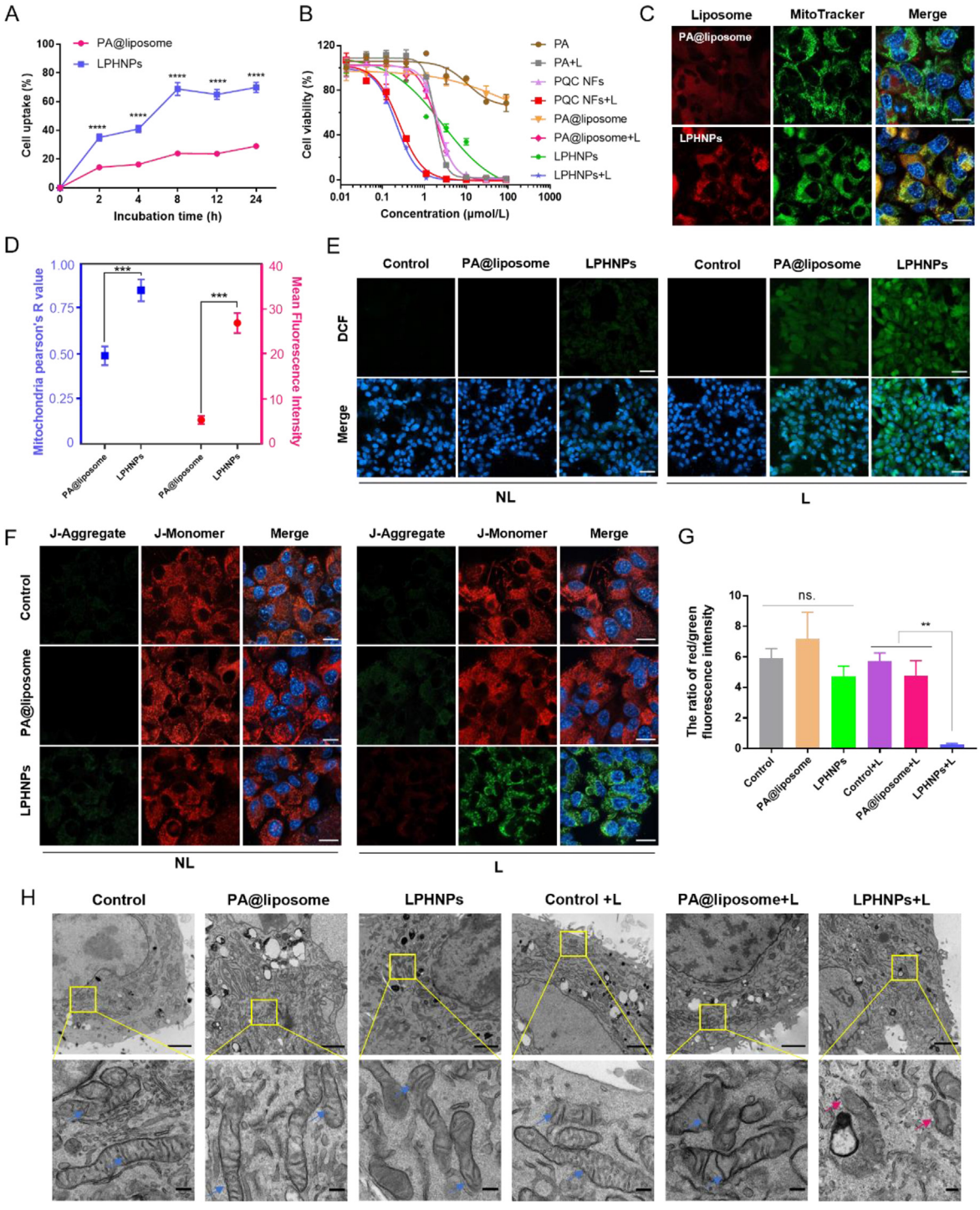

Figure 3 (A) Time-dependent uptake of PA@liposome and LPHNPs (1 μmol/L) in GL261 cells. (B) Viability curves of GL261 cells treated with PA, PQC NFs, PA@liposome and LPHNPs, with or without light irradiation. (C) Fluorescence colocalization of LPHNPs or PA@liposome (1 μmol/L) and mitochondria in GL261 cells. Cell nuclei were stained with Hoechst 33342. Scale bar = 20 μm. (D) Pearson correlation coefficient (Pearson's *R*) for colocalization analysis and the mean fluorescence intensity in (C). (E) Fluorescence imaging of ROS in GL261 cells treated as indicated (0.5 μmol/L). Cell nuclei were stained with Hoechst 33342. Scale bar = 50 μm. (F) JC-1 imaging for analysis of the mitochondrial membrane potential of cells that were treated as indicated. Cell nuclei were stained with Hoechst 33342. Scale bar = 20 μm. (G) Corresponding quantitative analysis of red to green fluorescence intensity ratio of cells in (G). (H) Representative TEM images of GL261 cells that were treated as indicated (0.5 μmol/L). Scale bar: 2 μm (upper panel) and 0.2 μm (lower panel). Arrows: mitochondria. NL: without light irradiation, L: with light irradiation. Light treatment was performed at a power density of 30 mW/cm^2 (633-nm LED array) for 30 s. Values are mean ± SD. Statistical analysis was performed with *t*-test, ns., not significant; $^{**}P < 0.01$; $^{***}P < 0.001$; $^{****}P < 0.0001$.

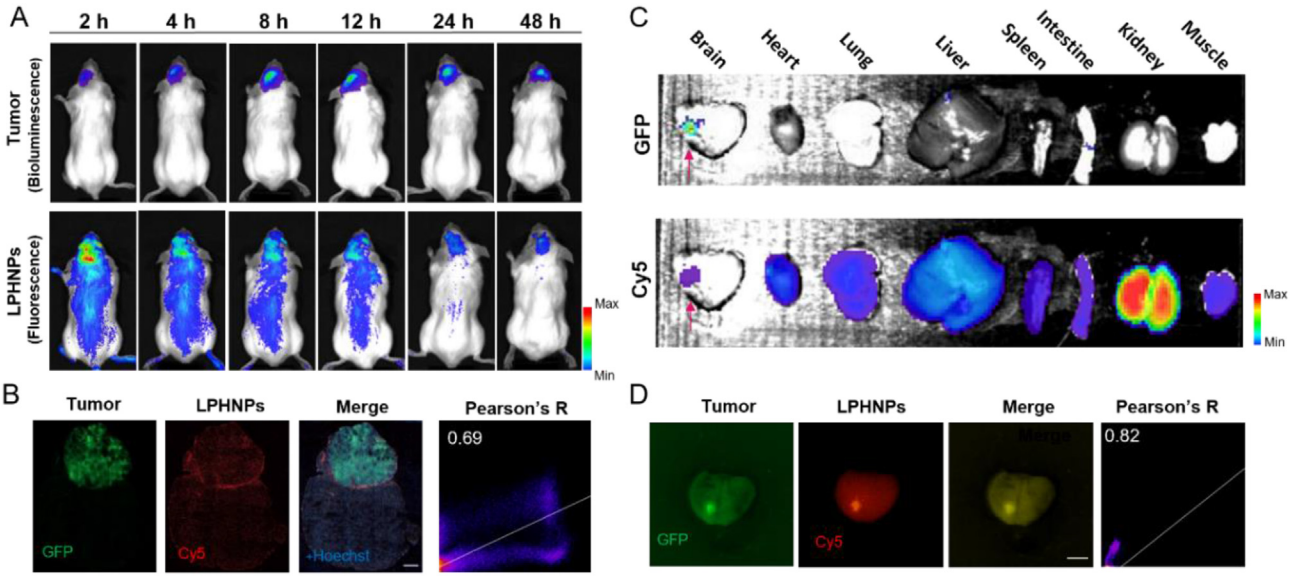

Figure 4 (A) Bioluminescence imaging of orthotopic GL261 tumors and fluorescence biodistribution of LPHNPs (10 mg/kg) in living mice at different time points after i. v. injection. (B) Confocal images of cryosection of harvested brain tissues from the orthotopic GL261 mouse model at 48 h post-injection with LPHNPs and calculated Pearson's *R* for colocalization analysis of GFP and Cy5 channel. Green: GL261-GFP, blue: Hoechst 33342, red: LPHNPs. Scale bar = 1 mm. (C) *Ex vivo* fluorescence imaging to show biodistribution of LPHNPs in the tumor and major organs. Arrows: tumor. (D) Multichannel fluorescence imaging of local brain bearing the orthotopic GL261 tumor and calculated Pearson's *R* for colocalization analysis of GFP and Cy5 channel. Green: GL261-GFP, red: LPHNPs. Scale bar = 4 mm.

S3d). Compared with the corresponding treatment groups without light, each group involved in light exposure showed increased antiproliferative activity against GL261 cells. Notably, among all groups, the light-activated LPHNPs and PQC NFs exhibited the most striking potency (IC_{50} = 0.21/0.25 μmol/L). Similar results were also obtained in other two human glioma cell lines, U251 and U118 (Figs. S3a and b). It is worth mentioning that no matter with or without light irradiation, LPHNPs formed from the co-assembly of lipid and PQC are equivalent in antiproliferative efficiency to PQC NFs formed by the self-assembly of PQC, indicating that the LPHNPs still preserve the properties of PQC NFs in the sub-localization and photosensitization inside cancer cells. Similar to PQC NFs, LPHNPs exhibited decreased cytotoxicity to the noncancerous IMR-90 cells compared with cancer cell lines, indicating that normal cell line is more tolerant to LPHNPs (Fig. S3c).

3.4. *Mitochondria targeting and MitoROS production*

The localization of photosensitizers in mitochondria is a key proponent of the compelling photodynamic anticancer effect of PQC NFs in cells[21]. To determine whether LPHNPs possess a comparable property of subcellular localization, the mitochondria colocalization study was conducted. GL261 cells were incubated with LPHNPs or PA@liposome, followed by staining with MitoTracker green. As shown in Fig. 3C and D, the red fluorescence of LPHNPs consistently overlapped with MitoTracker green, which contrasts sharply with the localization of PA@liposome and indicates that LPHNPs effectively deliver PQC molecules to mitochondria after uptake by cells. Since it has been verified that LPHNPs can target the mitochondria of cancer cells, we then explored their cellular photosensitization effects. The mitochondrial ROS (MitoROS) levels were measured by using MitoROS™580[30]. Compared with PA@liposome, LPHNPs significantly enhanced the generation of ROS in mitochondria after irradiation (Supporting Information Fig. S4a and b). Because the mitochondria are the main source of ROS, the enhanced MitoROS level would lead to excessive cellular ROS. By using 2′,7′-dichlorofluorescein diacetate (DCF-DA), we measured the cellular ROS. As shown in Fig. 3E and Fig. S4c, groups upon light treatment showed enhanced ROS production compared with the groups without light treatment. Moreover, LPHNPs with light irradiation dramatically induced ROS generation, while PA@liposome only exhibited a limited increase in ROS. This difference was attributed to the mitochondria targeting capacity and a higher cellular uptake of LPHNPs. Owing to the limited cellular uptake and lack of mitochondria-targeting ability, PA@liposome only showed a small amount of ROS production.

3.5. *Mitochondria dysfunction*

Mitochondrial membrane potential ($\Delta\psi_m$) is essential to mitochondrial functions, including driving ATP synthesis and keeping the balance of mitochondrial metabolism[31–33]. Decreased $\Delta\psi_m$ is a critical sign of mitochondrial dysfunction[34–36]. Thus, we detected the changes of $\Delta\psi_m$ by utilizing the JC-1 dye, which aggregates in mitochondria of normal $\Delta\psi_m$ and fluoresces red, and under low $\Delta\psi_m$ is dispersed to emit green fluorescence. Compared to the untreated group, LPHNPs with irradiation caused a significant decline in the ratio of red to green fluorescence intensity, indicating that the mitochondria treated with LPHNPs plus light have a decreased $\Delta\psi_m$ (Fig. 3F and G). To further visualize the effect of LPHNPs on mitochondrial microstructure, the cells that underwent different treatments were observed under TEM. As shown in Fig. 3H, mitochondria in the control and PA@liposome groups exhibited intact membrane structure, with the easily identifiable double membrane and arranged cristae. LPHNPs without light irradiation caused only a slight morphological change, indicating their mild activity in mitochondria. The

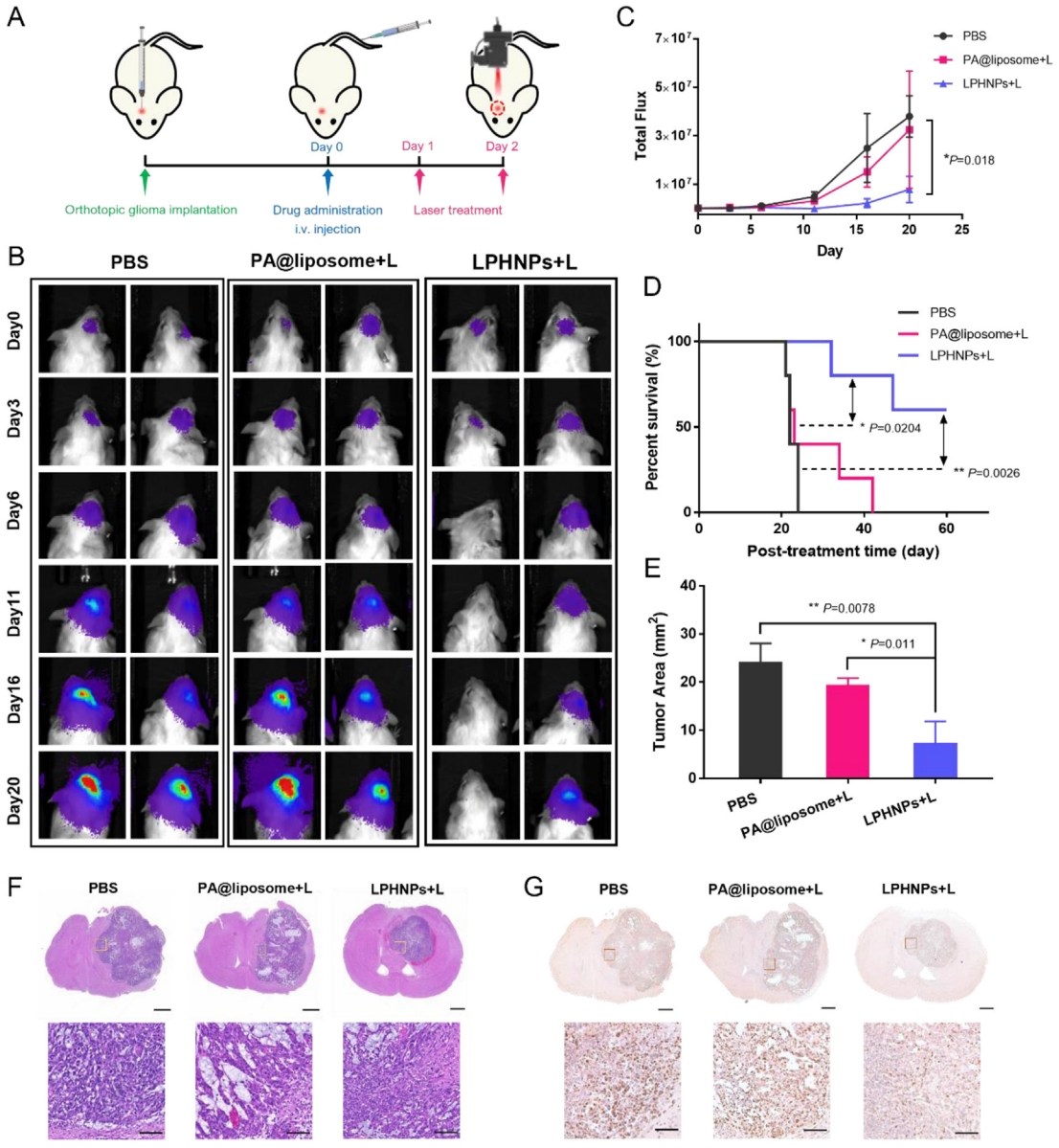

Figure 5 (A) Establishment of orthotopic GL261 model and treatment schedule with PBS, PA@liposome (10 mg/kg) with laser, LPHNPs (10 mg/kg) with laser. Laser dose was set as 0.2 W/cm^2 for 3 min. (B) Representative bioluminescence images of GL261-bearing mice treated with PBS, PA@liposome with laser and LPHNPs with laser, $n = 5$. (C) Quantitative data from bioluminescence imaging. (D) Kaplan−Meier survival curve of the GL261-bearing mice receiving the indicated treatments, $n = 5$. (E) Calculated tumor areas from H&E staining analysis of harvested brain tissues. (F) Representative of H&E staining analysis of the harvested brain tissues in which the heavily stained refers to the glioma area. Scale bar: 1 mm (upper panel), 0.1 mm (lower panel). (G) Representative of Ki67-IHC staining analysis of the harvested brain tissues. Scale bar:1 mm (upper panel), 0.1 mm (lower panel). Values are mean ± SD. Statistical analysis was performed with *t*-test, $*P < 0.05$, $**P < 0.01$.

mitochondria within LPHNPs and irradiation treatment displayed disintegrated membranes and cristae, while those treated with PA@liposome and light remained the distinguishable membrane structure. These data demonstrated that LPHNPs led to severe mitochondrial dysfunction by targeting mitochondria-targeted photodynamic effects.

3.6. *Apoptosis analysis*

Mitochondria play crucial roles in the programmed cell death[37]. The excess production of ROS in cells causes damage to mitochondria and further leads to the activation of cell death processes such as apoptosis[38,39]. Since LPHNPs induced a dramatic increase in ROS and led to mitochondrial dysfunction, we studied the proapoptotic effects of LPHNPs in cells. The apoptotic cell population was examined by using double staining with annexin V-FITC and propidium iodide. As shown in Supporting Information Fig. S5, only LPHNPs with light treatment induced a significant apoptotic population among all treatment groups, the Annexin V positive populations reached 39%. However, PA@liposome with light failed to cause apoptosis in cells, which may refer to its low concentration and limited uptake. LPHNPs without

light did not generate apoptotic cells, which indicated low cytotoxicity of LPHNPs in the absence of light.

3.7. Toxicity evaluation

To explore the systemic biocompatibility of LPHNPs, we assessed their safety in mice by monitoring body weight, hematology and pathological analysis. No significant body weight changes were observed after i.v. injection of 10 mg/kg LPHNPs for three weeks (Supporting Information Fig. S6). H&E staining showed that the histological patterns of major organs of LPHNPs treated mice are similar to those of the PBS group, indicating minimal systemic toxicity of LPHNPs. In addition, there were no obvious changes in the hematologic indexes found among the two groups. These results suggested that LPHNPs are tolerated in mice with i.v. administration.

3.8. Fluorescence imaging in vivo

To examine the application of LPHNPs in brain tumor imaging, an orthotopic glioma model was established by implanting GL261 cells expressing GFP and luciferase into the right striatum area of C57BL/6 mouse. Fluorescence imaging *in vivo* was conducted by monitoring the fluorescence of LPHNPs at different time intervals. Fig. 4A showed that LPHNPs circulated rapidly through the whole body and accumulated at the tumor sites in 2 h post-injection. Importantly, LPHNPs mainly distributed in the tumor sites at 48 h after injection, indicating their excellent tumor targeting capacity. The corresponding confocal imaging of cryo-sections exhibited overlapping between GL261 tumor (green) and LPHNPs (red, Fig. 4B). It is very interesting that hybrid nanoparticles without positive target function can accumulate at the brain tumor sites. It has been reported that dequalinium could facilitate the micelles to transport through the blood–brain barriers (BBB)[40,41]. Since dequalinium is a dimer of quinolinium, LPHNPs may have the similar ability to go through the BBB. In addition, the blood–brain tumor barrier (BBTB) of glioma has a large fenestration size and interendothelial gaps of 48 nm and 1 μm, respectively[42]. The process of engraftment maybe also compromises BBTB integrity[43]. Therefore, nano-sized LPHNPs could selectively accumulate in glioma tissue.

To further study the distribution of LPHNPs, the mice were sacrificed at 24 h post-injection to collect the major organs for *ex vivo* imaging. Fig. 4C and D showed that the fluorescent signals of LPHNPs highly overlapped with the GFP signals (the indicated tumor region), confirming the remarkable ability for brain tumor imaging of LPHNPs. The majority of collected organs showed low fluorescence signals, while the signals in kidneys were relatively high. This is likely due to the renal clearance pattern for porphyrin derivatives[44–46].

3.9. Antitumor efficacy in vivo

The therapeutic effect *in vivo* was evaluated by using the orthotopic GL261 model as well. Mice were randomly assigned into three groups ($n = 5$) and treated as indicated, followed by two laser treatments (0.2 W/cm^2, 3 min) at 24 and 48 h post-injection, respectively (Fig. 5A). As shown in Fig. 5B–D, PA@liposome with laser group negligibly inhibited tumor progression and did not prolong the overall survival time of mice compared to the PBS group showing progressively increased bioluminescence intensity. In contrast, LPHNPs with laser group significantly impeded tumor growth and extended overall survival outcome of animals (median survival, >60 days), as compared to the PBS group (median survival, 22 days) and PA@liposome with laser (median survival, 23 days). Importantly, three mice from the treatment group of LPHNPs plus laser survived longer than 60 days. Compared with other groups, the mice treated with LPHNPs and laser showed smaller tumor areas according to H&E staining (Fig. 5E and F). The Ki67-IHC showed the low proliferation activity of brain tissue treated with LPHNPs and laser (Fig. 5G). In addition, all groups didn't exhibit abnormalities in the histology of major organs, further indicating the safety of this hybrid nanoparticle *in vivo* (Supporting Information Fig. S7).

4. Conclusions

In this work, we developed a kind of mitochondria-targeting hybrid nanoparticles (LPHNPs) by engineering the co-assembly of the amphiphilic photosensitizer (PQC) and lipids as an efficient nanoplatform for imaging and therapy in an orthotopic glioma model. PQC was co-assembled with lipids to achieve an improved drug-loading rate that breaks through the limitation of conventional liposomes. Compared with the nanofiber self-assembled by PQC, LPHNPs preserved similar properties, including mitochondria-targeting capacity and photosensitization. In addition, the spherical nanostructure and desirable nanoscale of LPHNPs enabled PQC molecules to be administrated through i.v. injection. Due to the excellent mitochondria targeting capacity, LPHNPs with irradiation showed enhanced ROS and MitoROS production in cells and displayed ~10 times lower IC_{50} value than that of PA@liposome with irradiation. Comparatively, PA@liposome exhibited limited ROS production and efficiency of antiproliferation. Notably, the intrinsic fluorescence imaging capability of PQC could be utilized for the visualization of drug distribution *in vivo* and tumor imaging. Fluorescence imaging showed that LPHNPs accumulated in the tumor sites at 2 h post-injection and were retained for at least 48 h. *Ex vivo* imaging further confirmed the tumor targeting capacity of LPHNPs. In the orthotopic glioma model, a single dose of LPHNPs with laser treatment exhibited superior inhibition efficacy on tumor progression. More importantly, it significantly prolonged the survival of mice with orthotopic glioma.

The clinic data suggest potential beneficial effect of PDT for improving survival in glioma patients compared to standard therapy[47]. However, the application of PDT is hindered by the limited light penetration through the skull with an estimated effective therapeutic window restricted to 0.75−1.5 cm from the light source[47–49]. The initial therapeutic approach for glioma is surgery[50]. LPHNPs can be used as an effective photodynamic agent to eliminate the residue tumor cells after surgery when the skull is still opening. In addition, LPHNPs could be further modified through metal chelation to achieve positron emission tomography (PET) and magnetic resonance imaging (MRI). The simple preparation procedure, PDT therapeutic effect and *in vivo* imaging ability make this hybrid nanoparticle an ideal candidate for glioma imaging and treatment.

Acknowledgments

We thank the support from NIH/NCI (R01CA199668, R01CA232845), NIH/NIDCR (1R01DE029237, USA), NIH/NICHD (R01HD086195, USA), UC Davis Comprehensive Cancer Centre Support Grant (CCSG, USA) awarded by the National

Cancer Institute (NCI P30CA093373, USA). Cartoons in Fig. 1 were created with BioRender.com.

Author contributions

Yuanpei Li and Zhao Ma conceived the idea and designed the project. Menghuan Tang and Zhao Ma conducted all the experiments and data analyses. Kai Lin assisted with the chemical synthesis. Longmeng Li and Mythili Ramachandran assisted with animal studies. Menghuan Tang drafted and revised the paper. Zhao Ma, Mythili Ramachandran, Hongye Zou and Huzhi Zheng edited the paper. Zhao Ma and Yuanpei Li supervised the entire project and the overall paper preparation and revision.

Conflicts of interest

Yuanpei Li and Zhao Ma are the co-inventors on a pending patent application on the mitochondria targeting compounds and the resulting nanoformulations. The remaining authors declare no conflict of interest.

Appendix A. Supporting information

Supporting data to this article can be found online at https://doi.org/10.1016/j.apsb.2022.04.005.

References

1. Peetla C, Stine A, Labhasetwar V. Biophysical interactions with model lipid membranes: applications in drug discovery and drug delivery. *Mol Pharm* 2009;**6**:1264−76.
2. Martins S, Sarmento B, Ferreira DC, Souto EB. Lipid-based colloidal carriers for peptide and protein delivery—liposomes *versus* lipid nanoparticles. *Int J Nanomed* 2007;**2**:595−607.
3. Akbarzadeh A, Rezaei-Sadabady R, Davaran S, Joo SW, Zarghami N, Hanifehpour Y, et al. Liposome: classification, preparation, and applications. *Nanoscale Res Lett* 2013;**8**:102.
4. Blanken D, Foschepoth D, Serrao AC, Danelon C. Genetically controlled membrane synthesis in liposomes. *Nat Commun* 2020;**11**:4317.
5. Beltrán-Gracia E, López-Camacho A, Higuera-Ciapara I, Velázquez-Fernández JB, Vallejo-Cardona AA. Nanomedicine review: clinical developments in liposomal applications. *Cancer Nanotechnol* 2019;**10**:11.
6. Sercombe L, Veerati T, Moheimani F, Wu SY, Sood AK, Hua S. Advances and challenges of liposome assisted drug delivery. *Front Pharmacol* 2015;**6**:286.
7. Grimaldi N, Andrade F, Segovia N, Ferrer-Tasies L, Sala S, Veciana J, et al. Lipid-based nanovesicles for nanomedicine. *Chem Soc Rev* 2016;**45**:6520−45.
8. Ljubimova JY, Sun T, Mashouf L, Ljubimov AV, Israel LL, Ljubimov VA, et al. Covalent nano delivery systems for selective imaging and treatment of brain tumors. *Adv Drug Deliv Rev* 2017;**113**:177−200.
9. Wang L, Yang CQ, Wang J. Effects of loading procedures of magnetic nanoparticles on the structure and physicochemical properties of cisplatin magnetic liposomes. *J Microencapsul* 2012;**29**:781−9.
10. Cao J, Huang D, Peppas NA. Advanced engineered nanoparticulate platforms to address key biological barriers for delivering chemotherapeutic agents to target sites. *Adv Drug Deliv Rev* 2020;**167**:170−88.
11. Mukherjee A, Waters AK, Kalyan P, Achrol AS, Kesari S, Yenugonda VM. Lipid-polymer hybrid nanoparticles as a next-generation drug delivery platform: state of the art, emerging technologies, and perspectives. *Int J Nanomed* 2019;**14**:1937−52.
12. Vargas KM, Shon YS. Hybrid lipid−nanoparticle complexes for biomedical applications. *J Mater Chem B* 2019;**7**:695−708.
13. Jose C, Amra K, Bhavsar C, Momin M, Omri A. Polymeric lipid hybrid nanoparticles: properties and therapeutic applications. *Crit Rev Ther Drug* 2018;**35**:555−88.
14. Gopalakrishnan G, Danelon C, Izewska P, Prummer M, Bolinger PY, Geissbuhler I, et al. Multifunctional lipid/quantum dot hybrid nanocontainers for controlled targeting of live cells. *Angew Chem Int Ed* 2006;**45**:5478−83.
15. Lim YT, Noh YW, Cho JH, Han JH, Choi BS, Kwon J, et al. Multiplexed imaging of therapeutic cells with multispectrally encoded magnetofluorescent nanocomposite emulsions. *J Am Chem Soc* 2009;**131**:17145−54.
16. Thamphiwatana S, Gao WW, Pornpattananangkul D, Zhang QZ, Fu V, Li JY, et al. Phospholipase A2-responsive antibiotic delivery *via* nanoparticle-stabilized liposomes for the treatment of bacterial infection. *J Mater Chem B* 2014;**2**:8201−7.
17. Zhang XB, Li N, Zhang SW, Sun BJ, Chen Q, He ZG, et al. Emerging carrier-free nanosystems based on molecular self-assembly of pure drugs for cancer therapy. *Med Res Rev* 2020;**40**:1754−75.
18. Ma Z, Li J, Lin K, Ramachandran M, Zhang D, Showalter M, et al. Pharmacophore hybridisation and nanoscale assembly to discover self-delivering lysosomotropic new-chemical entities for cancer therapy. *Nat Commun* 2020;**11**:4615.
19. Wang HX, Lu ZJ, Wang LJ, Guo TT, Wu JP, Wan JQ, et al. New generation nanomedicines constructed from self-assembling small-molecule prodrugs alleviate cancer drug toxicity. *Cancer Res* 2017;**77**:6963−74.
20. Fontana F, Figueiredo P, Zhang P, Hirvonen JT, Liu DF, Santos HA. Production of pure drug nanocrystals and nano co-crystals by confinement methods. *Adv Drug Deliv Rev* 2018;**131**:3−21.
21. Lin K, Ma Z, Li J, Tang M, Lindstrom A, Ramachandran M, et al. Single small molecule-assembled mitochondria targeting nanofibers for enhanced photodynamic cancer therapy *in vivo*. *Adv Funct Mater* 2020;**31**:2008460.
22. Zhang HW. Thin-film hydration followed by extrusion method for liposome preparation. *Methods Mol Biol* 2017;**1522**:17−22.
23. Bangham AD, Horne RW. Negative staining of phospholipids and their structural modification by surface-active agents as observed in the electron microscope. *J Mol Biol* 1964;**8**:660−8.
24. Hong YN, Lam JWY, Tang BZ. Aggregation-induced emission: phenomenon, mechanism and applications. *Chem Commun* 2009;**29**:4332−53.
25. Li Y, Lin TY, Luo Y, Liu Q, Xiao W, Guo W, et al. A smart and versatile theranostic nanomedicine platform based on nanoporphyrin. *Nat Commun* 2014;**5**:4712.
26. Cheng HB, Li YY, Tang BZ, Yoon J. Assembly strategies of organic-based imaging agents for fluorescence and photoacoustic bioimaging applications. *Chem Soc Rev* 2020;**49**:21−31.
27. Noh I, Lee D, Kim H, Jeong CU, Lee Y, Ahn JO, et al. Enhanced photodynamic cancer treatment by mitochondria-targeting and brominated near-infrared fluorophores. *Adv Sci (Weinh)* 2018;**5**:1700481.
28. Honary S, Zahir F. Effect of zeta potential on the properties of nano-drug delivery systems—a review (Part 1). *Trop J Pharmaceut Res* 2013;**12**:255−64.
29. Arias-Alpizar G, Kong L, Vlieg RC, Rabe A, Papadopoulou P, Meijer MS, et al. Light-triggered switching of liposome surface charge directs delivery of membrane impermeable payloads *in vivo*. *Nat Commun* 2020;**11**:3638.
30. Cho H, Cho YY, Shim MS, Lee JY, Lee HS, Kang HC. Mitochondria-targeted drug delivery in cancers. *Bba-Mol Basis Dis* 2020;**1866**:165808.
31. Logan A, Pell VR, Shaffer KJ, Evans C, Stanley NJ, Robb EL, et al. Assessing the mitochondrial membrane potential in cells and *in vivo* using targeted click chemistry and mass spectrometry. *Cell Metabol* 2016;**23**:379−85.
32. Zorova LD, Popkov VA, Plotnikov EY, Silachev DN, Pevzner IB, Jankauskas SS, et al. Mitochondrial membrane potential. *Anal Biochem* 2018;**552**:50−9.

33. Murphy MP, Hartley RC. Mitochondria as a therapeutic target for common pathologies. *Nat Rev Drug Discov* 2018;**17**:865−86.
34. Murphy MP. How mitochondria produce reactive oxygen species. *Biochem J* 2009;**417**:1−13.
35. Ly JD, Grubb DR, Lawen A. The mitochondrial membrane potential (deltapsi(m)) in apoptosis; an update. *Apoptosis* 2003;**8**:115−28.
36. de la Mata M, Cotan D, Villanueva-Paz M, de Lavera I, Alvarez-Cordoba M, Luzon-Hidalgo R, et al. Mitochondrial dysfunction in lysosomal storage disorders. *Diseases* 2016;**4**:31.
37. Zimmermann KC, Bonzon C, Green DR. The machinery of programmed cell death. *Pharmacol Therapeut* 2001;**92**:57−70.
38. Ott M, Gogvadze V, Orrenius S, Zhivotovsky B. Mitochondria, oxidative stress and cell death. *Apoptosis* 2007;**12**:913−22.
39. Fleury C, Mignotte B, Vayssière JL. Mitochondrial reactive oxygen species in cell death signaling. *Biochimie* 2002;**84**:131−41.
40. Pan Y, Zhao S, Chen F. The potential value of dequalinium chloride in the treatment of cancer: focus on malignant glioma. *Clin Exp Pharmacol Physiol* 2021;**48**:445−54.
41. Ju RJ, Mu LM, Li XT, Li CQ, Cheng ZJ, Lu WL. Development of functional docetaxel nanomicelles for treatment of brain glioma. *Artif Cell Nanomed Biotechnol* 2018;**46**:1180−90.
42. Xin HL, Jiang Y, Lv W, Xu JP. Liposome-based drug delivery for brain tumor theranostics. In: Kesharwani P, Gupta U, editors. *Nanotechnology-based targeted drug delivery systems for brain tumors*. Elsevier; 2018. p. 245−66.
43. Genovesi LA, Puttick S, Millar A, Kojic M, Ji P, Lagendijk AK, et al. Patient-derived orthotopic xenograft models of medulloblastoma lack a functional blood−brain barrier. *Neuro Oncol* 2021;**23**:732−42.
44. Bayona AMD, Mroz P, Thunshelle C, Hamblin MR. Design features for optimization of tetrapyrrole macrocycles as antimicrobial and anticancer photosensitizers. *Chem Biol Drug Des* 2017;**89**:192−206.
45. Huang HY, Hernandez R, Geng JM, Sun HT, Song WT, Chen F, et al. A porphyrin-PEG polymer with rapid renal clearance. *Biomaterials* 2016;**76**:25−32.
46. Cheng L, Jiang D, Kamkaew A, Valdovinos HF, Im HJ, Feng L, et al. Renal-clearable PEGylated porphyrin nanoparticles for image-guided photodynamic cancer therapy. *Adv Funct Mater* 2017;**27**:1702928.
47. Cramer SW, Chen CC. Photodynamic therapy for the treatment of glioblastoma. *Front Surg* 2019;**6**:81.
48. Bechet D, Mordon SR, Guillemin F, Barberi-Heyob MA. Photodynamic therapy of malignant brain tumours: a complementary approach to conventional therapies. *Cancer Treat Rev* 2014;**40**:229−41.
49. Akimoto J, Haraoka J, Aizawa K. Preliminary clinical report on safety and efficacy of photodynamic therapy using talaporfin sodium for malignant gliomas. *Photodiagn Photodyn* 2012;**9**:91−9.
50. Taylor OG, Brzozowski JS, Skelding KA. Glioblastoma multiforme: an overview of emerging therapeutic targets. *Front Oncol* 2019;**9**:963.